

A FAST SOLVER FOR ELASTIC SCATTERING FROM AXISYMMETRIC OBJECTS BY BOUNDARY INTEGRAL EQUATIONS

JUN LAI AND HEPING DONG

ABSTRACT. Fast and high-order accurate algorithms for three dimensional elastic scattering are of great importance when modeling physical phenomena in mechanics, seismic imaging, and many other fields of applied science. In this paper, we develop a novel boundary integral formulation for the three dimensional elastic scattering based on the Helmholtz decomposition of elastic fields, which converts the Navier equation to a coupled system consisted of Helmholtz and Maxwell equations. An FFT-accelerated separation of variables solver is proposed to efficiently invert boundary integral formulations of the coupled system for elastic scattering from axisymmetric rigid bodies. In particular, by combining the regularization properties of the singular boundary integral operators and the FFT-based fast evaluation of modal Green's functions, our numerical solver can rapidly solve the resulting integral equations with a high-order accuracy. Several numerical examples are provided to demonstrate the efficiency and accuracy of the proposed algorithm, including geometries with corners at different wave number.

1. INTRODUCTION

Recently the phenomena of elastic scattering by obstacles have received much attention due to the significant applications in various scientific areas such as geological exploration, nondestructive testing, and medical diagnostics [3, 31]. An accurate and efficient numerical method plays an important role in many of these applications. For instance, in the area of inverse elastic scattering, a large amount of forward simulations are needed in the iterative-type inversion algorithm [13, 14]. This paper is concerned with the elastic scattering of a time-harmonic incident wave by a rigid obstacle embedded in a homogeneous and isotropic elastic medium in three dimensions. We propose a novel boundary integral formulation for the governing equation, that is, the Navier equation, and develop a highly accurate numerical method for solving the elastic scattering problem from axisymmetric bodies.

Given the importance of elasticity, there are many mathematical and computational results available for the scattering problems of elastic waves [1, 38, 39, 41]. Among these results, the method of boundary integral equations offers an attractive approach for solving the obstacle scattering problems. Not only does it provide many analytic insights for the solution of elastic scattering, from the computational point of view, it also has the advantages that the discretization is only needed on the boundary of the domain and the radiation condition at infinity can be satisfied automatically [41]. On the other hand, the Green's function of the elastic wave equation is a second order tensor and the singularity is rather tedious to be separated in the computation of boundary integral equations, especially for the three dimensional case. Readers are referred to [4, 9, 39, 42] and reference therein for some recent advances along this direction. To bypass this complexity, we use the Helmholtz decomposition to introduce two potential functions, one scalar and one vector, to split the displacement

Date: April 9, 2021.

2020 Mathematics Subject Classification. 35J05, 45L05, 45E05, 65R20, 75B05.

Key words and phrases. elastic wave scattering, boundary integral equations, Nyström method, Helmholtz decomposition, Navier equations.

The work of JL was partially supported by the Funds for Creative Research Groups of NSFC (No. 11621101) and NSFC grant No. 11871427. The work of HD was partially supported by NSFC grant No. 11801213 and the National Key Research and Development Program of China (grant No. 2020YFA0713602).

of the elastic wave fields into the compressional wave and the shear wave. The two potential functions, where the scalar one satisfies the Helmholtz equation and the vector one satisfies the Maxwell equation, are only coupled at the boundary of the obstacle [15]. Therefore, the boundary value problem of the Navier equation is converted equivalently into a coupled boundary value problem of Helmholtz and Maxwell equations for the potentials. Such a decomposition greatly reduces the complexity of computation for the elastic scattering problem, as many numerical techniques available for the boundary integral formulations for Helmholtz and Maxwell equations can be directly applied to the coupled problem, including the Fast Multiple Method (FMM) [19, 21]. Applications of this technique in two dimensional multi-particle scattering and inverse elastic scattering can be found in [13, 14, 35].

While in practice many elastic scattering problems require the solution to Navier equations in arbitrary complex geometries, it is also important to study the scattering problems in somewhat simpler geometries, namely axisymmetric ones. Despite they simplify the persistent mathematical and computational difficulties of designing high-order methods in general geometries (e.g. quadrature design, mesh generation, etc), many practical problems, such as submarine detection, can be approximately modeled as the elastic scattering of axisymmetric objects. They can also provide a robust test-bed for the same integral equations which are used in general geometries and serve as building blocks for more complex objects, including composite materials made by axisymmetric particles [19, 24]. In fact, the problem of computing scattered waves in axisymmetric geometries has a very rich history in both the acoustic and electromagnetic wave scattering communities [17, 22, 44], and recently several groups have built specialized high-order solvers for particular applications in plasma physics [40], resonance calculations [27, 28], and inverse obstacle scattering [5]. However, we are not aware of any efficient algorithm for the elastic scattering from axisymmetric objects.

In this work, based on the Helmholtz decomposition, the elastic scattered field decomposes into the gradient of a Helmholtz potential and the curl of a Maxwell potential. We represent them by the Helmholtz and Maxwell single layer potentials, respectively. (The definition of Maxwell single layer potential will be given in Section 3.) By using the boundary condition, we obtain a coupled integral equation system that consists of four singular boundary operators. It will be shown that two of them are only weakly singular after extracting the jumping terms, while the other two have Cauchy-type singularities. In order to design a high order discretization algorithm, we investigate the regularization properties of the two Cauchy-type singular operators, which will be reduced to weakly singular operators only, and then apply the integral formulation to the scattering problem of axisymmetric objects. To evaluate the singular operators efficiently, we use a fast Fourier transform (FFT) based scheme to accelerate the evaluation of so-called modal Green's functions, which has been successfully applied in a variety of boundary value problems including Laplace equations, Helmholtz equations [43], and recently, Maxwell's equations [27, 36]. Numerical results show that at the low frequency case, our algorithm can finish the computation in a few seconds on a laptop and achieve 10 digits accuracy compared with the reference solution. For the high frequency case, we are also able to get more than 6 digits accuracy in a reasonable amount of time. In addition, high order accuracy is also obtained for axisymmetric bodies that contain corners by using an adaptive discretization scheme. In summary, our work in this paper has three main features: (1) a novel integral formulation for the elastic scattering problem based on Helmholtz decomposition, (2) new regularization properties for the singular integral operators resulted from the coupled boundary integral system, (3) a fast and high order discretization scheme for the elastic scattering of axisymmetric objects based on FFT.

We also make a few remarks on the integral formulation we choose. Analogous to the single, double and combined layer potential representations for the Helmholtz equations [32], one can also construct three variants for the integral representation of Navier equations. The integral formulation we adopt does not admit a unique solution in certain cases, as explained in Section 3. However, it does not

undermine the value of the proposed algorithm, as the extension to the other two formulations would be straightforward.

An outline of the paper is the following: Section 2 introduces the problem of Navier equations for the time-harmonic elastic scattering in isotropic media. Section 3 formulates the boundary integral equation system and shows the regularization properties of the singular operators. Section 4 gives the transformation of the integral equation along an axisymmetric surface into a sequence of decoupled integral equations along a curve in two dimensions based on the Fourier transform in the azimuthal direction. Ideas for the fast kernel evaluation by FFT are given in Section 5. It also discusses the high-order discretization of the sequence of line integrals using adaptive panels and generalized Gaussian quadratures for the associated weakly singular integral operators. Numerical examples are given in Section 6, including scattering results in both smooth and non-smooth geometries. Section 7 concludes the discussion with some future work.

2. PROBLEM FORMULATION

Consider a three-dimensional rigid obstacle Ω , given as a simply connected, bounded domain in \mathbb{R}^3 with boundary Γ . To ease the discussion, we assume the boundary Γ is smooth, although it will be numerically extended to non-smooth geometries. Denote by $\boldsymbol{\tau}_1, \boldsymbol{\tau}_2$ and \mathbf{n} the unit tangential and exterior normal vectors on Γ , respectively. The exterior domain $\mathbb{R}^3 \setminus \overline{\Omega}$ is assumed to be filled with a homogeneous and isotropic elastic medium with a unit mass density.

Let the obstacle be illuminated by a time-harmonic compressional plane wave $\mathbf{u}^{\text{inc}}(\mathbf{x}) = (\mathbf{d} \cdot \mathbf{p}) \mathbf{d} e^{i\kappa_p \mathbf{d} \cdot \mathbf{x}}$ or shear plane wave $\mathbf{u}^{\text{inc}}(\mathbf{x}) = (\mathbf{d} \times \mathbf{p}) \times \mathbf{d} e^{i\kappa_s \mathbf{d} \cdot \mathbf{x}}$, where \mathbf{d} and \mathbf{p} are the propagation and polarization vectors, respectively, both of which are vectors on a unit sphere, and

$$\kappa_p = \frac{\omega}{\sqrt{\lambda + 2\mu}}, \quad \kappa_s = \frac{\omega}{\sqrt{\mu}},$$

are the compressional wavenumber and shear wavenumber, respectively. Here $\omega > 0$ is the angular frequency and λ, μ are the Lamé constants satisfying $\mu > 0, \lambda + \mu > 0$. The displacement of the total elastic field \mathbf{u} satisfies the Navier equation

$$\mu \Delta \mathbf{u} + (\lambda + \mu) \nabla \nabla \cdot \mathbf{u} + \omega^2 \mathbf{u} = 0 \quad \text{in } \mathbb{R}^3 \setminus \overline{\Omega}.$$

Since the obstacle is assumed to be rigid, it implies \mathbf{u} satisfies the homogeneous boundary condition

$$\mathbf{u} = 0 \quad \text{on } \Gamma.$$

The total field \mathbf{u} consists of the incident field \mathbf{u}^{inc} and the scattered field \mathbf{u}^{sc} , i.e.,

$$\mathbf{u} = \mathbf{u}^{\text{inc}} + \mathbf{u}^{\text{sc}}.$$

It is easy to verify that the incoming field \mathbf{u}^{inc} satisfies the Navier equation. Therefore the scattered field \mathbf{u}^{sc} satisfies the boundary value problem

$$\begin{cases} \mu \Delta \mathbf{u}^{\text{sc}} + (\lambda + \mu) \nabla \nabla \cdot \mathbf{u}^{\text{sc}} + \omega^2 \mathbf{u}^{\text{sc}} = 0 & \text{in } \mathbb{R}^3 \setminus \overline{\Omega}, \\ \mathbf{u}^{\text{sc}} = -\mathbf{u}^{\text{inc}} & \text{on } \Gamma. \end{cases} \quad (1)$$

In order to guarantee the well-posedness of the corresponding boundary value problem, the field \mathbf{u}^{sc} is required to satisfy the Kupradze radiation condition at infinity, i.e.

$$\lim_{r \rightarrow \infty} r(\partial_r \mathbf{u}_p - i\kappa_p \mathbf{u}_p) = 0, \quad \lim_{r \rightarrow \infty} r(\partial_r \mathbf{u}_s - i\kappa_s \mathbf{u}_s) = 0, \quad r = |\mathbf{x}|, \quad (2)$$

uniformly in all directions, where

$$\mathbf{u}_p = -\frac{1}{\kappa_p^2} \nabla \nabla \cdot \mathbf{u}^{\text{sc}}, \quad \mathbf{u}_s = \frac{1}{\kappa_s^2} \nabla \times \nabla \times \mathbf{u}^{\text{sc}}$$

are known as the compressional and shear wave components of \mathbf{u}^{sc} , respectively.

While there exists the free space Green's function for the Navier equation, we choose to apply the Helmholtz decomposition to formulate the integral equation for the boundary value problem (1). As we mentioned in the introduction, such a decomposition will simplify the computation of elastic scattering. For any solution \mathbf{u}^{sc} of the elastic wave equation (1), the Helmholtz decomposition reads

$$\mathbf{u}^{\text{sc}} = \nabla\varphi + \nabla \times \boldsymbol{\psi}, \quad \text{with } \nabla \cdot \boldsymbol{\psi} = 0, \quad (3)$$

where φ and $\boldsymbol{\psi}$ are scalar and vector potentials, respectively. Combining (1) and (3) yields the Helmholtz and Maxwell equations

$$\begin{cases} \Delta\varphi + \kappa_{\text{p}}^2\varphi = 0, \\ \nabla \times \nabla \times \boldsymbol{\psi} - \kappa_{\text{s}}^2\boldsymbol{\psi} = 0. \end{cases} \quad (4)$$

Due to the Kupradze radiation condition (2), φ and $\boldsymbol{\psi}$ are required to satisfy the Sommerfeld radiation conditions

$$\lim_{r \rightarrow \infty} r(\partial_r \varphi - i\kappa_{\text{p}}\varphi) = 0, \quad \lim_{r \rightarrow \infty} r(\partial_r \boldsymbol{\psi} - i\kappa_{\text{s}}\boldsymbol{\psi}) = 0, \quad r = |\mathbf{x}|,$$

while the second equality is understood in the sense of component-wise, and is equivalent to the Silver-Müller radiation condition in electromagnetic scattering [12]. The coupling between φ and $\boldsymbol{\psi}$ follows from the boundary condition on Γ that

$$\mathbf{u}^{\text{sc}} = \nabla\varphi + \nabla \times \boldsymbol{\psi} = -\mathbf{u}^{\text{inc}}.$$

Taking the dot and cross products of the above equation with the normal vector \mathbf{n} , respectively, we obtain

$$\partial_{\mathbf{n}}\varphi + \mathbf{n} \cdot \nabla \times \boldsymbol{\psi} = f, \quad \mathbf{n} \times \varphi + \mathbf{n} \times \nabla \times \boldsymbol{\psi} = \mathbf{g},$$

where

$$f = -\mathbf{n} \cdot \mathbf{u}^{\text{inc}}, \quad \mathbf{g} = -\mathbf{n} \times \mathbf{u}^{\text{inc}}.$$

In summary, the potential functions φ and $\boldsymbol{\psi}$ satisfy the coupled boundary value problem

$$\begin{cases} \Delta\varphi + \kappa_{\text{p}}^2\varphi = 0, & \nabla \times \nabla \times \boldsymbol{\psi} - \kappa_{\text{s}}^2\boldsymbol{\psi} = 0, & \text{in } \mathbb{R}^3 \setminus \overline{\Omega}, \\ \partial_{\mathbf{n}}\varphi + \mathbf{n} \cdot \nabla \times \boldsymbol{\psi} = f, & \mathbf{n} \times \nabla\varphi + \mathbf{n} \times \nabla \times \boldsymbol{\psi} = \mathbf{g}, & \text{on } \Gamma, \\ \lim_{r \rightarrow \infty} r(\partial_r \varphi - i\kappa_{\text{p}}\varphi) = 0, & \lim_{r \rightarrow \infty} r(\partial_r \boldsymbol{\psi} - i\kappa_{\text{s}}\boldsymbol{\psi}) = 0, & r = |\mathbf{x}|. \end{cases} \quad (5)$$

When $\kappa_{\text{p}} > 0$ and $\kappa_{\text{s}} > 0$, the uniqueness result of the coupled system (5) can be obtained by standard argument [35]. We assume this always holds in the subsequent discussion, and mainly focus on solving system (5) by the integral equation method.

3. INTEGRAL EQUATION FORMULATIONS

Using potential theory, we can represent the potential functions φ and $\boldsymbol{\psi}$ in (4) by

$$\varphi = S^{\kappa_{\text{p}}}\sigma, \quad \boldsymbol{\psi} = \frac{1}{\kappa_{\text{s}}^2} \nabla \times \nabla \times S^{\kappa_{\text{s}}}\mathbf{J}, \quad \text{for } \mathbf{x} \in \mathbb{R}^3 \setminus \overline{\Omega}, \quad (6)$$

where

$$S^{\kappa_{\text{p}}}\sigma(\mathbf{x}) = \int_{\Gamma} G^{\kappa_{\text{p}}}(\mathbf{x}, \mathbf{y})\sigma(\mathbf{y})ds_{\mathbf{y}}, \quad (7)$$

$$S^{\kappa_{\text{s}}}\mathbf{J}(\mathbf{x}) = \int_{\Gamma} G^{\kappa_{\text{s}}}(\mathbf{x}, \mathbf{y})\mathbf{J}(\mathbf{y})ds_{\mathbf{y}}, \quad (8)$$

and the function $G^{\kappa}(\mathbf{x}, \mathbf{y})$ is the free space Green's function for the three dimensional Helmholtz equation:

$$G^{\kappa}(\mathbf{x}, \mathbf{y}) = \frac{e^{i\kappa|\mathbf{x}-\mathbf{y}|}}{4\pi|\mathbf{x}-\mathbf{y}|}, \quad \kappa = \kappa_{\text{p}} \text{ OR } \kappa_{\text{s}}, \quad (9)$$

σ is the unknown charge density and \mathbf{J} is the unknown *surface current* (as a terminology used in electromagnetic scattering) on Γ . While the representation for φ is the well-known Helmholtz single layer potential, for convenience we call the representation for $\boldsymbol{\psi}$ in (6) as the *Maxwell single layer potential*. Based on the identity

$$\frac{1}{\kappa_s^2} \nabla \times \nabla \times S^{\kappa_s} \mathbf{J} = \frac{1}{\kappa_s^2} \nabla \nabla \cdot S^{\kappa_s} \mathbf{J} - \frac{1}{\kappa_s^2} \Delta S^{\kappa_s} \mathbf{J} = \frac{1}{\kappa_s^2} \nabla \nabla \cdot S^{\kappa_s} \mathbf{J} + S^{\kappa_s} \mathbf{J}, \quad (10)$$

the solution \mathbf{u}^{sc} can be represented by

$$\mathbf{u}^{sc} = \nabla \varphi + \nabla \times \boldsymbol{\psi} = \nabla S^{\kappa_p} \sigma + \nabla \times S^{\kappa_s} \mathbf{J}. \quad (11)$$

To derive the integral equation, we need the limiting behavior of the integral operators, since when \mathbf{x} approaches the boundary Γ , the integrals φ and $\boldsymbol{\psi}$ become singular. Denote by $C^{0,\alpha}(\Gamma)$, $0 < \alpha < 1$, the classic *Hölder space*, which is a Banach space with the norm

$$\|\sigma\|_{0,\alpha} := \sup_{\mathbf{x} \in \Gamma} |\sigma(\mathbf{x})| + \sup_{\mathbf{x}, \mathbf{y} \in \Gamma, \mathbf{x} \neq \mathbf{y}} \frac{|\sigma(\mathbf{x}) - \sigma(\mathbf{y})|}{|\mathbf{x} - \mathbf{y}|^\alpha}.$$

Let $C^{1,\alpha}(\Gamma)$ be the Banach space with the norm

$$\|\sigma\|_{1,\alpha} := \sup_{\mathbf{x} \in \Gamma} |\sigma(\mathbf{x})| + \sup_{\mathbf{x} \in \Gamma} \|\nabla \sigma\|_{0,\alpha}.$$

Following the notation in [12], we denote by $T^{0,\alpha}(\Gamma)$, $0 < \alpha < 1$, the space of all uniformly Hölder continuous tangential fields on Γ , and define $T_d^{0,\alpha}(\Gamma)$ to be the Banach space

$$T_d^{0,\alpha}(\Gamma) = \{\mathbf{J} \in T^{0,\alpha}(\Gamma) : \text{Div} \mathbf{J} \in C^{0,\alpha}(\Gamma)\},$$

where Div denotes the surface divergence on Γ .

Lemma 3.1. *For the single layer potential φ in equation (7) with density $\sigma \in C^{0,\alpha}(\Gamma)$, the first derivative can be uniformly Hölder continuously extended from $\mathbb{R}^3 \setminus \overline{\Omega}$ to $\mathbb{R}^3 \setminus \Omega$ with boundary value*

$$\nabla \varphi_+(\mathbf{x}) = \int_{\Gamma} \nabla_{\mathbf{x}} G^{\kappa}(\mathbf{x}, \mathbf{y}) \sigma(\mathbf{y}) ds_{\mathbf{y}} - \frac{1}{2} \sigma(\mathbf{x}) \mathbf{n}(\mathbf{x}), \quad \mathbf{x} \in \Gamma$$

where

$$\nabla \varphi_+ := \lim_{h \rightarrow +0} \nabla \varphi(\mathbf{x} + h \mathbf{n}(x)).$$

Here we denote by $\nabla_{\mathbf{x}}$ the gradient with respect to \mathbf{x} . Proof can be found in [12](Theorem 3.3)

Lemma 3.2. *For the vector potential $\boldsymbol{\psi}$ in equation (8) with density $\mathbf{J} \in T^{0,\alpha}(\Gamma)$, the first derivative can be uniformly Hölder continuously extended from $\mathbb{R}^3 \setminus \overline{\Omega}$ to $\mathbb{R}^3 \setminus \Omega$ with boundary value*

$$\nabla \times \boldsymbol{\psi}_+(\mathbf{x}) = \int_{\Gamma} \nabla_{\mathbf{x}} G^{\kappa}(\mathbf{x}, \mathbf{y}) \times \mathbf{J}(\mathbf{y}) ds_{\mathbf{y}} - \frac{1}{2} \mathbf{n}(\mathbf{x}) \times \mathbf{J}(\mathbf{x}), \quad \mathbf{x} \in \Gamma$$

where

$$\nabla \times \boldsymbol{\psi}_+ := \lim_{h \rightarrow +0} \nabla \times \boldsymbol{\psi}(\mathbf{x} + h \mathbf{n}(x)).$$

Proof can be found in [12](Theorem 6.12)

By making use of the two lemmas above, we are able to formulate the integral equations by letting \mathbf{x} approach the boundary Γ from the exterior, which yields the system

$$\begin{cases} (-\frac{1}{2} + \mathcal{K}) \sigma(\mathbf{x}) + \mathcal{N} \mathbf{J}(\mathbf{x}) = f(\mathbf{x}), \\ \mathcal{H} \sigma(\mathbf{x}) + (\frac{1}{2} + \mathcal{M}) \mathbf{J}(\mathbf{x}) = \mathbf{g}(\mathbf{x}), \end{cases} \quad \mathbf{x} \in \Gamma, \quad (12)$$

where

$$\begin{aligned}\mathcal{K}\sigma(\mathbf{x}) &= \int_{\Gamma} \mathbf{n}(\mathbf{x}) \cdot \nabla_{\mathbf{x}} G^{\kappa_{\text{p}}}(\mathbf{x}, \mathbf{y}) \sigma(\mathbf{y}) ds_{\mathbf{y}}, & \mathcal{N}\mathbf{J}(\mathbf{x}) &= \int_{\Gamma} \mathbf{n}(\mathbf{x}) \cdot \nabla_{\mathbf{x}} \times (G^{\kappa_{\text{s}}}(\mathbf{x}, \mathbf{y}) \mathbf{J}(\mathbf{y})) ds_{\mathbf{y}}, \\ \mathcal{H}\sigma(\mathbf{x}) &= \int_{\Gamma} \mathbf{n}(\mathbf{x}) \times \nabla_{\mathbf{x}} G^{\kappa_{\text{p}}}(\mathbf{x}, \mathbf{y}) \sigma(\mathbf{y}) ds_{\mathbf{y}}, & \mathcal{M}\mathbf{J}(\mathbf{x}) &= \int_{\Gamma} \mathbf{n}(\mathbf{x}) \times \nabla_{\mathbf{x}} \times (G^{\kappa_{\text{s}}}(\mathbf{x}, \mathbf{y}) \mathbf{J}(\mathbf{y})) ds_{\mathbf{y}}.\end{aligned}$$

While all the four boundary integral operators in (12) are defined in the sense of Cauchy principle value, the operators \mathcal{K} and \mathcal{M} are only weakly singular for smooth surface Γ . Therefore they can be numerically discretized by the generalized Gaussian quadrature. Details will be given in Section 5. In order to discretize the operators \mathcal{H} and \mathcal{N} to high order, we need the following regularization properties.

Theorem 3.3. *Let $\boldsymbol{\tau}_1$ and $\boldsymbol{\tau}_2$ be the unit tangential vectors of a closed C^2 surface Γ and $\mathbf{n} = \boldsymbol{\tau}_1 \times \boldsymbol{\tau}_2$. For $\sigma \in C^{1,\alpha}(\Gamma)$, $0 < \alpha < 1$ and $i = 1, 2$, it holds*

$$\begin{aligned}\int_{\Gamma} \frac{\partial G^{\kappa}(\mathbf{x}, \mathbf{y})}{\partial \boldsymbol{\tau}_i(\mathbf{x})} \sigma(\mathbf{y}) ds_{\mathbf{y}} &= \int_{\Gamma} G^{\kappa}(\mathbf{x}, \mathbf{y}) \text{Div}_{\mathbf{y}}(\mathbf{n}(\mathbf{y}) \times \boldsymbol{\tau}_i(\mathbf{x}) \times \mathbf{n}(\mathbf{y})) \sigma(\mathbf{y}) ds_{\mathbf{y}} \\ &+ \int_{\Gamma} G^{\kappa}(\mathbf{x}, \mathbf{y}) (\mathbf{n}(\mathbf{y}) \times \boldsymbol{\tau}_i(\mathbf{x}) \times \mathbf{n}(\mathbf{y})) \cdot \text{Grad}_{\mathbf{y}} \sigma(\mathbf{y}) ds_{\mathbf{y}} \\ &- \boldsymbol{\tau}_i(\mathbf{x}) \cdot \int_{\Gamma} \frac{\partial G^{\kappa}(\mathbf{x}, \mathbf{y})}{\partial \mathbf{n}(\mathbf{y})} \mathbf{n}(\mathbf{y}) \sigma(\mathbf{y}) ds_{\mathbf{y}}\end{aligned}\quad (13)$$

for $\mathbf{x} \in \Gamma$, where $\text{Div}_{\mathbf{y}}$ and $\text{Grad}_{\mathbf{y}}$ are the surface divergence and gradient on Γ with respect to \mathbf{y} , respectively.

Proof. For $i = 1, 2$, based on the identity $\nabla_{\mathbf{x}} G^{\kappa}(\mathbf{x}, \mathbf{y}) = -\nabla_{\mathbf{y}} G^{\kappa}(\mathbf{x}, \mathbf{y})$, the operator

$$\begin{aligned}\int_{\Gamma} \frac{\partial G^{\kappa}(\mathbf{x}, \mathbf{y})}{\partial \boldsymbol{\tau}_i(\mathbf{x})} \sigma(\mathbf{y}) ds_{\mathbf{y}} &= - \int_{\Gamma} \boldsymbol{\tau}_i \cdot \nabla_{\mathbf{y}} G^{\kappa}(\mathbf{x}, \mathbf{y}) \sigma(\mathbf{y}) ds_{\mathbf{y}} \\ &= - \int_{\Gamma} \boldsymbol{\tau}_i(\mathbf{x}) \cdot \left(\text{Grad}_{\mathbf{y}} G^{\kappa}(\mathbf{x}, \mathbf{y}) + \mathbf{n}(\mathbf{y}) \frac{\partial G^{\kappa}(\mathbf{x}, \mathbf{y})}{\partial \mathbf{n}(\mathbf{y})} \right) \sigma(\mathbf{y}) ds_{\mathbf{y}} \\ &= - \int_{\Gamma} (\mathbf{n}(\mathbf{y}) \times \boldsymbol{\tau}_i(\mathbf{x}) \times \mathbf{n}(\mathbf{y})) \cdot \text{Grad}_{\mathbf{y}} G^{\kappa}(\mathbf{x}, \mathbf{y}) \sigma(\mathbf{y}) ds_{\mathbf{y}} \\ &- \boldsymbol{\tau}_i(\mathbf{x}) \cdot \int_{\Gamma} \frac{\partial G^{\kappa}(\mathbf{x}, \mathbf{y})}{\partial \mathbf{n}(\mathbf{y})} \mathbf{n}(\mathbf{y}) \sigma(\mathbf{y}) ds_{\mathbf{y}},\end{aligned}$$

The conclusion follows from the two identities:

$$\int_{\Gamma} \mathbf{J} \cdot \text{Grad} \sigma ds_{\mathbf{y}} = - \int_{\Gamma} \sigma \text{Div} \mathbf{J} ds_{\mathbf{y}}, \quad (14)$$

$$\text{Div}(\sigma \mathbf{J}) = \text{Grad} \sigma \cdot \mathbf{J} + \sigma \text{Div} \mathbf{J} \quad (15)$$

for any function $\sigma \in C^{1,\alpha}(\Gamma)$ and tangential vector $\mathbf{J} := J^1 \boldsymbol{\tau}_1 + J^2 \boldsymbol{\tau}_2 \in T_d^{0,\alpha}(\Gamma)$. \square

Theorem 3.4. *Let $\boldsymbol{\tau}_1$ and $\boldsymbol{\tau}_2$ be the unit tangential vectors of a closed C^2 surface Γ and $\mathbf{n} = \boldsymbol{\tau}_1 \times \boldsymbol{\tau}_2$. For $\mathbf{n} \times \mathbf{J} = -J^2 \boldsymbol{\tau}_1 + J^1 \boldsymbol{\tau}_2 \in T_d^{0,\alpha}(\Gamma)$, $0 < \alpha < 1$, and $i = 1, 2$, it holds*

$$\begin{aligned}\mathbf{n}(\mathbf{x}) \cdot \nabla_{\mathbf{x}} \times \int_{\Gamma} G^{\kappa}(\mathbf{x}, \mathbf{y}) \mathbf{J}(\mathbf{y}) ds_{\mathbf{y}} &= - \int_{\Gamma} G^{\kappa}(\mathbf{x}, \mathbf{y}) \text{Grad}_{\mathbf{y}}(\mathbf{n}(\mathbf{x}) \cdot \mathbf{n}(\mathbf{y})) \cdot (\mathbf{n}(\mathbf{y}) \times \mathbf{J}(\mathbf{y})) ds_{\mathbf{y}} \\ &- \int_{\Gamma} G^{\kappa}(\mathbf{x}, \mathbf{y}) \mathbf{n}(\mathbf{x}) \cdot \mathbf{n}(\mathbf{y}) \text{Div}_{\mathbf{y}}(\mathbf{n}(\mathbf{y}) \times \mathbf{J}(\mathbf{y})) ds_{\mathbf{y}} \\ &- \mathbf{n}(\mathbf{x}) \cdot \int_{\Gamma} \frac{\partial G^{\kappa}(\mathbf{x}, \mathbf{y})}{\partial \mathbf{n}(\mathbf{y})} \mathbf{n}(\mathbf{y}) \times \mathbf{J}(\mathbf{y}) ds_{\mathbf{y}},\end{aligned}\quad (16)$$

for $\mathbf{x} \in \Gamma$.

Proof. The operator

$$\begin{aligned}
& \mathbf{n}(\mathbf{x}) \cdot \nabla_{\mathbf{x}} \times \int_{\Gamma} G^{\kappa}(\mathbf{x}, \mathbf{y}) \mathbf{J}(\mathbf{y}) ds_{\mathbf{y}} \\
&= \mathbf{n}(\mathbf{x}) \cdot \int_{\Gamma} \nabla_{\mathbf{x}} G^{\kappa}(\mathbf{x}, \mathbf{y}) \times \mathbf{J}(\mathbf{y}) ds_{\mathbf{y}} \\
&= \int_{\Gamma} \nabla_{\mathbf{y}} G^{\kappa}(\mathbf{x}, \mathbf{y}) \cdot \mathbf{n}(\mathbf{x}) \times \mathbf{J}(\mathbf{y}) ds_{\mathbf{y}} \\
&= \int_{\Gamma} \left(\text{Grad}_{\mathbf{y}} G^{\kappa}(\mathbf{x}, \mathbf{y}) + \mathbf{n}(\mathbf{y}) \frac{\partial G^{\kappa}(\mathbf{x}, \mathbf{y})}{\partial \mathbf{n}(\mathbf{y})} \right) \cdot \mathbf{n}(\mathbf{x}) \times \mathbf{J}(\mathbf{y}) ds_{\mathbf{y}} \\
&= - \int_{\Gamma} G^{\kappa}(\mathbf{x}, \mathbf{y}) \text{Div}_{\mathbf{y}} (\mathbf{n}(\mathbf{y}) \times (\mathbf{n}(\mathbf{x}) \times \mathbf{J}(\mathbf{y})) \times \mathbf{n}(\mathbf{y})) ds_{\mathbf{y}} - \mathbf{n}(\mathbf{x}) \cdot \int_{\Gamma} \frac{\partial G^{\kappa}(\mathbf{x}, \mathbf{y})}{\partial \mathbf{n}(\mathbf{y})} \mathbf{n}(\mathbf{y}) \times \mathbf{J}(\mathbf{y}) ds_{\mathbf{y}}
\end{aligned}$$

Here the last equality is obtained by making use of the identity (14). Combining identity (15), we further have

$$\begin{aligned}
& \text{Div}_{\mathbf{y}} (\mathbf{n}(\mathbf{y}) \times (\mathbf{n}(\mathbf{x}) \times \mathbf{J}(\mathbf{y})) \times \mathbf{n}(\mathbf{y})) \\
&= \text{Div}_{\mathbf{y}} ((\mathbf{n}(\mathbf{x}) \cdot \mathbf{n}(\mathbf{y}) J^1(\mathbf{y})) \boldsymbol{\tau}_2(\mathbf{y}) - (\mathbf{n}(\mathbf{x}) \cdot \mathbf{n}(\mathbf{y}) J^2(\mathbf{y})) \boldsymbol{\tau}_1(\mathbf{y})) \\
&= \text{Grad}_{\mathbf{y}} (\mathbf{n}(\mathbf{x}) \cdot \mathbf{n}(\mathbf{y})) \cdot (-J^2 \boldsymbol{\tau}_1 + J^1 \boldsymbol{\tau}_2) + \mathbf{n}(\mathbf{x}) \cdot \mathbf{n}(\mathbf{y}) \text{Div}_{\mathbf{y}} (-J^2 \boldsymbol{\tau}_1 + J^1 \boldsymbol{\tau}_2)
\end{aligned}$$

which completes the proof. \square

Based on Theorems 3.3 and 3.4, we can transform the Cauchy-type singular operators \mathcal{H} and \mathcal{N} into operators with weak singularities only, which greatly simplify the numerical computation. In the next section, we will make use of these results and discuss the Fourier expansions of these operators along the azimuthal direction of the axisymmetric boundary Γ .

Remark 3.5. *Although the original boundary value problem (5) has a unique solution for $\kappa_{\mathbf{p}} > 0$ and $\kappa_{\mathbf{s}} > 0$, the integral formulation (12) based on the single layer potentials (6) does not admit a unique solution when $\kappa_{\mathbf{p}}$ is the eigenvalue of the interior Helmholtz Dirichlet problem or $\kappa_{\mathbf{s}}$ is the eigenvalue of the interior Maxwell problem with zero tangential electric field on Γ . Detailed analysis for the two dimensional case can be found in [35].*

Remark 3.6. *Another way to represent the potential functions φ and $\boldsymbol{\psi}$ is given by*

$$\varphi = D^{\kappa_{\mathbf{p}}} \sigma, \quad \boldsymbol{\psi} = \nabla \times S^{\kappa_{\mathbf{s}}} \mathbf{J}, \quad \text{for } \mathbf{x} \in \mathbb{R}^3 \setminus \overline{\Omega}, \quad (17)$$

where

$$D^{\kappa_{\mathbf{p}}} \sigma(\mathbf{x}) = \int_{\Gamma} \frac{\partial G^{\kappa_{\mathbf{p}}}(\mathbf{x}, \mathbf{y})}{\partial \mathbf{n}(\mathbf{y})} \sigma(\mathbf{y}) ds_{\mathbf{y}},$$

which does not admit a unique solution either when $\kappa_{\mathbf{p}}$ is the eigenvalue of the interior Helmholtz Neumann problem or $\kappa_{\mathbf{s}}$ is the eigenvalue of the interior Maxwell problem with zero tangential magnetic field on Γ .

Remark 3.7. *To eliminate the resonance frequency, one can apply the combined field technique to represent φ and $\boldsymbol{\psi}$ as*

$$\begin{cases} \varphi = (D^{\kappa_{\mathbf{p}}} + i\lambda_0 S^{\kappa_{\mathbf{p}}}) \sigma, \\ \boldsymbol{\psi} = \left(\nabla \times S^{\kappa_{\mathbf{s}}} + \frac{i\lambda_0}{\kappa_{\mathbf{s}}^2} \nabla \times \nabla \times S^{\kappa_{\mathbf{s}}} \right) \mathbf{J}, \end{cases} \quad \text{for } \mathbf{x} \in \mathbb{R}^3 \setminus \overline{\Omega}, \quad (18)$$

for some $\lambda_0 > 0$. However, since in this work we mainly focus on the high order numerical method for the elastic scattering from axisymmetric objects, we simply adopt the single layer representation (6) by assuming that $\kappa_{\mathbf{p}}$ is not the eigenvalue of the interior Helmholtz Dirichlet problem and $\kappa_{\mathbf{s}}$ is not the eigenvalue of the interior Maxwell problem. Extension of the algorithm to the integral representation (17) and the combined field representation (18) will be straightforward but tedious. In

particular, we will need the regularization properties of three dimensional hypersingular operators. Details will be explored in the future work.

Remark 3.8. *Although our numerical scheme focuses on the axisymmetric bodies, the integral formulation (12), as well as the regularization results in Theorems 3.3 and 3.4, are applicable to general geometries with closed boundaries.*

4. FOURIER REPRESENTATION OF THE BOUNDARY INTEGRAL OPERATORS

It is an area of active research to discretize integral equations in complex geometries in three dimensions to high order, which is highly non-trivial and rather computationally expensive [7]. Some recent progress in this area can be found in [20]. However, there exist many important applications of elastic scattering from axisymmetric objects (for instance, submarine detection, composite materials, etc). In this case, variables can be separated in cylindrical coordinates resulting in a system of decoupled line integrals. The discretization and solution of integral equations along curves in two dimensions is a much easier problem, and there exist many efficient schemes [2, 6, 23, 25]. In addition, the resulting Fourier decomposition scheme easily parallelizes and can address a range of rather complicated axisymmetric geometries. Discussion and details regarding the discretization of scalar-valued integral equations along bodies of revolution are contained in [26, 43]. The vector-valued case, in particular integral equation methods for Maxwell's equations, are discussed in [27, 36]. In this section, we follow the discussion and notations in [34, 36] to Fourier expand the operators in (12).

Consider an axisymmetric object Ω with rotational symmetry with respect to the z -axis. In other words, its boundary Γ is generated by rotating curve γ in the xz -plane about the z -axis. The goal is to design an efficient numerical solver for the time-harmonic Navier equations with the rigid boundary conditions along the surface of axisymmetric objects, given in terms of the boundary integral system (12). It is convenient to consider the problem in cylindrical coordinates, which will be given as (r, θ, z) , and we denote the standard unit vectors by $(\mathbf{e}_r, \mathbf{e}_\theta, \mathbf{e}_z)$. We assume that the generating curve γ is parameterized counterclockwise by $(r(s), z(s))$, where s denotes arclength. This implies that the unit tangential vector along the generating curve is $\mathbf{t}(s) = r'(s) \mathbf{e}_r + z'(s) \mathbf{e}_z$, with r' and z' denoting differentiation with respect to arclength. It is assumed that the generating curve γ is smooth or contains a small number of corners. The unit tangential vectors on Γ are given by $(\mathbf{t}, \mathbf{e}_\theta)$. The unit exterior normal \mathbf{n} is then given by $\mathbf{n}(s) = z'(s) \mathbf{e}_r - r'(s) \mathbf{e}_z$. Since the cross section of Γ in the azimuthal direction is a circle, the density function σ can be expanded in terms of the Fourier series with respect to θ ,

$$\sigma(r, \theta, z) = \sum_m \sigma_m(r, z) e^{im\theta}. \quad (19)$$

Similarly, the surface current \mathbf{J} on Γ can be written as $\mathbf{J} = J^1 \mathbf{t} + J^2 \mathbf{e}_\theta$. Taking the Fourier expansion of J^1 and J^2 with respect to θ yields

$$\mathbf{J}(r, \theta, z) = \sum_m (J_m^1(r, z) \mathbf{t} + J_m^2(r, z) \mathbf{e}_\theta) e^{im\theta}. \quad (20)$$

In the following, the dependence of the unit vectors on the variables r, θ, z will be omitted unless needed for clarity.

For numerical purpose, we need to investigate the Fourier expansions of the singular operators \mathcal{K} , \mathcal{N} , \mathcal{H} and \mathcal{M} in terms of the Fourier coefficients of σ and \mathbf{J} given in (19) and (20). Let

$(r_t, \theta_t, z_t) = (r(t), \theta(t), z(t))$ be a target point on Γ . Define the modal Green's functions as

$$g_m^{\kappa,1}(r_t, z_t, r, z) = \int_0^{2\pi} \frac{e^{i\kappa\rho}}{4\pi\rho} e^{-im\varphi} d\varphi, \quad (21)$$

$$g_m^{\kappa,2}(r_t, z_t, r, z) = \int_0^{2\pi} \frac{e^{i\kappa\rho}}{4\pi\rho} \cos m\varphi \cos \varphi d\varphi, \quad (22)$$

$$g_m^{\kappa,3}(r_t, z_t, r, z) = \int_0^{2\pi} \frac{e^{i\kappa\rho}}{4\pi\rho} \sin m\varphi \sin \varphi d\varphi, \quad (23)$$

where

$$\rho = \sqrt{r_t^2 + r^2 - 2r_t r \cos \varphi + (z_t - z)^2}, \quad (24)$$

$\varphi = \theta_t - \theta$ and $\kappa = \kappa_p$ or κ_s .

We begin by the Fourier expansion of single layer potentials.

Lemma 4.1. *The single layer potential $S^\kappa \sigma$ in cylindrical coordinate has the Fourier expansion*

$$S^\kappa \sigma(r_t, \theta_t, z_t) = \sum_m \beta_m(r_t, z_t) e^{im\theta_t} \quad (25)$$

where

$$\beta_m^\kappa(r_t, z_t) = \int_\gamma \sigma_m(s) r(s) g_m^{\kappa,1}(r_t, z_t, r(s), z(s)) ds. \quad (26)$$

It is obtained by direct computation, which is also given in [43, 26]. From Lemma 4.1, the Fourier expansion for the boundary operator $\mathcal{K}\sigma$ with respect to the azimuthal direction is given as

$$\mathcal{K}\sigma(r_t, \theta_t, z_t) = \sum_m \left(z_t' \frac{\partial \beta_m^{\kappa_p}}{\partial r_t} - r_t' \frac{\partial \beta_m^{\kappa_p}}{\partial z_t} \right) e^{im\theta_t}. \quad (27)$$

where we denote the gradient of γ at (r_t, z_t) as $\nabla\gamma(t) = (r_t', z_t')$.

Lemma 4.2. *The vector potential $S^\kappa \mathbf{J}$ in cylindrical coordinate has the Fourier expansion*

$$S^\kappa \mathbf{J}(r_t, \theta_t, z_t) = \sum_m (c_m^{\kappa,1}(r_t, z_t) \mathbf{e}_r + c_m^{\kappa,2}(r_t, z_t) \mathbf{e}_\theta + c_m^{\kappa,3}(r_t, z_t) \mathbf{e}_z) e^{im\theta_t} \quad (28)$$

where

$$\begin{aligned} c_m^{\kappa,1}(r_t, z_t) &= \int_\gamma J_m^1(s) r(s) r'(s) g_m^{\kappa,2}(r_t, z_t, r(s), z(s)) ds \\ &\quad - i \int_\gamma J_m^2(s) r(s) g_m^{\kappa,3}(r_t, z_t, r(s), z(s)) ds, \\ c_m^{\kappa,2}(r_t, z_t) &= i \int_\gamma J_m^1(s) r(s) r'(s) g_m^{\kappa,3}(r_t, z_t, r(s), z(s)) ds \\ &\quad + \int_\gamma J_m^2(s) r(s) g_m^{\kappa,2}(r_t, z_t, r(s), z(s)) ds, \\ c_m^{\kappa,3}(r_t, z_t) &= \int_\gamma J_m^1(s) r(s) z'(s) g_m^{\kappa,1}(r_t, z_t, r(s), z(s)) ds. \end{aligned}$$

Using Lemma 4.2, we can obtain the azimuthal Fourier decomposition of the boundary operator $\mathcal{M}\mathbf{J}$:

$$\begin{aligned} \mathcal{M}\mathbf{J}(r_t, \theta_t, z_t) = & \\ \sum_m \left(\left(\frac{\partial c_m^{\kappa_s, 1}}{\partial z_t} - \frac{\partial c_m^{\kappa_s, 3}}{\partial r_t} \right) \mathbf{t} - \left(\frac{z'_t}{r_t} \left(c_m^{\kappa_s, 2} + r_t \frac{\partial c_m^{\kappa_s, 2}}{\partial r_t} - i m c_m^{\kappa_s, 1} \right) + r'_t \left(\frac{i m}{r_t} c_m^{\kappa_s, 3} - \frac{\partial c_m^{\kappa_s, 2}}{\partial z_t} \right) \right) \mathbf{e}_\theta \right) e^{i m \theta_t}. \end{aligned} \quad (29)$$

In order to derive the Fourier representations of boundary operators \mathcal{H} and \mathcal{N} , by Theorems 3.3 and 3.4, we need the Fourier expansions of the double layer boundary operators

$$\mathcal{D}^\kappa(\sigma \mathbf{n})(\mathbf{x}) = \int_\Gamma \frac{\partial G^\kappa(\mathbf{x}, \mathbf{y})}{\partial \mathbf{n}(\mathbf{y})} \mathbf{n}(\mathbf{y}) \sigma(\mathbf{y}) ds_{\mathbf{y}} \quad (30)$$

$$\mathcal{D}^\kappa(\mathbf{n} \times \mathbf{J})(\mathbf{x}) = \int_\Gamma \frac{\partial G^\kappa(\mathbf{x}, \mathbf{y})}{\partial \mathbf{n}(\mathbf{y})} \mathbf{n}(\mathbf{y}) \times \mathbf{J}(\mathbf{y}) ds_{\mathbf{y}} \quad (31)$$

for $\mathbf{x} \in \Gamma$, $\kappa = \kappa_p$ or κ_s , $\sigma \in C^{1, \alpha}(\Gamma)$ and $\mathbf{J} \in T^{0, \alpha}(\Gamma)$. For brevity, we drop the dependence on $(r_t, z_t, r(s), z(s))$ for all the derivatives of $g_m^{\kappa, i}$, $i = 1, 2, 3$.

Lemma 4.3. *The double layer boundary operator $\mathcal{D}^\kappa(\sigma \mathbf{n})$ in cylindrical coordinate has the Fourier expansion*

$$\mathcal{D}^\kappa(\sigma \mathbf{n})(r_t, \theta_t, z_t) = \sum_m (a_m^{\kappa, 1}(r_t, z_t) \mathbf{e}_r + a_m^{\kappa, 2}(r_t, z_t) \mathbf{e}_\theta + a_m^{\kappa, 3}(r_t, z_t) \mathbf{e}_z) e^{i m \theta_t} \quad (32)$$

where

$$\begin{aligned} a_m^{\kappa, 1}(r_t, z_t) &= \int_\gamma \sigma_m(s) r(s) z'(s) \left(z'(s) \frac{\partial g_m^{\kappa, 2}}{\partial r} - r'(s) \frac{\partial g_m^{\kappa, 2}}{\partial z} \right) ds \\ a_m^{\kappa, 2}(r_t, z_t) &= i \int_\gamma \sigma_m(s) r(s) z'(s) \left(z'(s) \frac{\partial g_m^{\kappa, 3}}{\partial r} - r'(s) \frac{\partial g_m^{\kappa, 3}}{\partial z} \right) ds \\ a_m^{\kappa, 3}(r_t, z_t) &= - \int_\gamma \sigma_m(s) r'(s) r(s) \left(z'(s) \frac{\partial g_m^{\kappa, 1}}{\partial r} - r'(s) \frac{\partial g_m^{\kappa, 1}}{\partial z} \right) ds \end{aligned}$$

Lemma 4.4. *The double layer boundary operator $\mathcal{D}^\kappa(\mathbf{n} \times \mathbf{J})$ in cylindrical coordinate has the Fourier expansion*

$$\mathcal{D}^\kappa(\mathbf{n} \times \mathbf{J})(r_t, \theta_t, z_t) = \sum_m (b_m^{\kappa, 1}(r_t, z_t) \mathbf{e}_r + b_m^{\kappa, 2}(r_t, z_t) \mathbf{e}_\theta + b_m^{\kappa, 3}(r_t, z_t) \mathbf{e}_z) e^{i m \theta_t} \quad (33)$$

where

$$\begin{aligned}
b_m^{\kappa,1}(r_t, z_t) &= \int_{\gamma} J_m^2(s) r(s) r'(s) \left(z'(s) \frac{\partial g_m^{\kappa,2}}{\partial r} - r'(s) \frac{\partial g_m^{\kappa,2}}{\partial z} \right) ds \\
&\quad + i \int_{\gamma} J_m^1(s) r(s) \left(z'(s) \frac{\partial g_m^{\kappa,3}}{\partial r} - r'(s) \frac{\partial g_m^{\kappa,3}}{\partial z} \right) ds, \\
b_m^{\kappa,2}(r_t, z_t) &= i \int_{\gamma} J_m^2(s) r(s) r'(s) \left(z'(s) \frac{\partial g_m^{\kappa,3}}{\partial r} - r'(s) \frac{\partial g_m^{\kappa,3}}{\partial z} \right) ds \\
&\quad - \int_{\gamma} J_m^1(s) r(s) \left(z'(s) \frac{\partial g_m^{\kappa,2}}{\partial r} - r'(s) \frac{\partial g_m^{\kappa,2}}{\partial z} \right) ds, \\
b_m^{\kappa,3}(r_t, z_t) &= \int_{\gamma} J_m^2(s) r(s) z'(s) \left(z'(s) \frac{\partial g_m^{\kappa,1}}{\partial r} - r'(s) \frac{\partial g_m^{\kappa,1}}{\partial z} \right) ds.
\end{aligned}$$

For the other components in the right hand sides of formulae (13) and (16), their Fourier representations can be found by combining Lemmas 4.1, 4.2 and the Fourier expansions of surface gradient and divergence for axisymmetric shape Γ , which are given in the appendix. From these expansions, one can see that in order to evaluate the boundary operators \mathcal{K} , \mathcal{N} , \mathcal{H} and \mathcal{M} rapidly, the values of $a_m^{\kappa,1}$, $b_m^{\kappa,2}$ and $c_m^{\kappa,3}$, $i = 1, 2, 3$, as well as the derivatives of $c_m^{\kappa,3}$, need to be computed efficiently. The evaluation of these coefficients can be performed in two steps: (1) Compute $g_m^{\kappa,i}$ and its derivatives, and then (2) integrate $g_m^{\kappa,i}$ and its derivatives (according to the above formulae) along the generating curve γ . Unfortunately, there are no numerically useful closed-form expressions for $g_m^{\kappa,i}$. Expansions of these functions in terms of half-order Hankel functions are expensive to compute [11] and designing robust contour integration methods for large values of m is quite complicated [22]. Furthermore, since $g_m^{\kappa,i}$ has a logarithmic singularity when $(r_t, z_t) = (r(s), z(s))$, special care must be taken during the integration along γ . Direct evaluation based on the adaptive integration has been proven to be time consuming and will be the bottleneck of the resulting solver [34]. Therefore, an efficient numerical scheme is needed to accelerate the two steps. Here we adopt an FFT based algorithm for the evaluation of $g_m^{\kappa,i}$ (as well as their derivatives), and apply the generalized Gaussian quadrature for the singular integration along γ . To avoid redundancy of the existing work, we only introduce some general ideas in the next section and refer interested readers to [26, 36, 43] for more details.

5. FAST KERNEL EVALUATION AND GENERALIZED GAUSSIAN QUADRATURE

5.1. Fast kernel evaluation. To evaluate the modal Green's functions (21)-(23), including their derivatives, we adopt the method based on FFT, recurrence relations and kernel splitting, as discussed in [16, 25, 26], to accelerate the computation of these kernel functions.

Based on the fact that ρ in equation (24) is an even function with respect to φ on $[0, 2\pi]$, we observe that

$$g_m^{\kappa,2} = \frac{g_{m+1}^{\kappa,1} + g_{m-1}^{\kappa,1}}{2}, \quad g_m^{\kappa,3} = -\frac{g_{m+1}^{\kappa,1} - g_{m-1}^{\kappa,1}}{2} \quad (34)$$

for any mode m . In other words, we need only to evaluate $g_m^{\kappa,1}$ and its derivatives efficiently, as the other two kernel functions can be obtained by linear combinations (34). Therefore the goal is to efficiently evaluate all $g_m^{\kappa,1}$ for $|m| \leq M$, where $M > 0$ is the bandwidth of the data in the azimuthal direction. In general, unless the wave numbers κ_p and κ_s are particularly high, only a modest number of Fourier modes m are needed for high-precision discretizations of the integral equations. Once the incoming data has been Fourier transformed along the azimuthal direction on the boundary, the

number of Fourier modes M needed in the discretization can be determined based on the decay of the coefficients of the incoming field.

The evaluation of $g_m^{\kappa,1}$ for $|m| \leq M$ can be split into two cases. To ease the discussion, we let $(r(s), z(s))$ be replaced by (r_s, z_s) for simplicity.

- (1) When the target (r_t, z_t) is far away from the source (r_s, z_s) , the integral in (21) can be discretized using the periodic trapezoidal rule with $2M + 1$ -points and therefore the fast Fourier transform (FFT) can be used to evaluate all the $g_m^{\kappa,1}$ for $m = -M, -M + 1, \dots, M$.
- (2) When (r_t, z_t) is near (r_s, z_s) , the integrand is nearly singular and a prohibitively large number of discretization points would be needed to obtain sufficient quadrature accuracy. To overcome this difficulty, we apply the kernel splitting technique. The main idea is to explicitly split the integrand into smooth and singular parts. Fourier coefficients of the smooths parts can be obtained numerically via the FFT. The coefficients of the singular part can be obtained analytically via recurrence relations. The Fourier coefficients of the original kernel can then be obtained via discrete convolution. It has been successfully applied in [16, 26, 36, 43], and therefore we skip the details that are given in the reference mentioned. In particular, [16] provides estimates on the size of the FFT needed and other important tuning parameters.

Finally, it is easy to show that in both cases, the computational complexity is $\mathcal{O}(M \log M)$, which implies the scheme is highly efficient.

5.2. Generalized Gaussian quadrature. Once a scheme to evaluate the modal Green's functions and their derivatives is in place, the next step is to discretize each decoupled modal integral equation along the generating curve γ . Here we use a Nyström-like method for discretizing the integral equations. Since the modal Green's functions have logarithmic singularities [10, 11], any efficient Nyström-like scheme will require a quadrature that accurately evaluates weakly singular integral operators. For high order integration, one can construct the quadrature based on the kernel splitting technique as in [32]. However, this will become tedious given the various order of singularities in the derivatives of $g_m^{\kappa,i}$. For our numerical simulations, we implement a panel-based discretization scheme using generalized Gaussian quadratures. An in-depth discussion of generalized Gaussian quadrature schemes is given in [8, 23]. The panel-based discretization scheme of this paper, as opposed to that based on hybrid-Gauss trapezoidal rules [2, 16, 40], allows for adaptive discretizations. Application of this panel-based discretization to the electromagnetic scattering from axisymmetric surfaces in three dimensions with edges and corners can be found in [36].

More specifically, given a kernel function g with logarithmic singularity and smooth function σ , our goal is to evaluate, with high-order accuracy, the integral

$$\mathcal{S}\sigma(\mathbf{x}) = \int_{\gamma} g(\mathbf{x}, \mathbf{y}) \sigma(\mathbf{y}) ds_{\mathbf{y}}. \quad (35)$$

Assume that the generating curve γ is smooth and parametrized as $\gamma(s)$, where s is the arclength. The total arclength will be denoted by L . We first divide $[0, L]$ into N panels. The division can be either uniform or nonuniform, depending on the particular geometry. Each of the N panels, and therefore any function supported on it, is discretized using p scaled Gauss-Legendre nodes. In a Nyström discretization scheme, the layer potential above is approximated given as

$$\mathcal{S}\sigma(\mathbf{x}_{lm}) \approx \sum_{i=1}^N \sum_{j=1}^p w_{lmij} g(\mathbf{x}_{lm}, \mathbf{y}_{ij}) \sigma(\mathbf{y}_{ij}), \quad (36)$$

where \mathbf{x}_{lm} is the m th Gauss-Legendre node on panel l , \mathbf{y}_{ij} is the j th Gauss-Legendre node on panel i , and w_{lmij} is the Nyström quadrature weight. For singular integrals, it is generally difficult to have a uniform quadrature for all \mathbf{x}_{lm} . We therefore split the integral (35) into two parts and consider

them separately, i.e.

$$\mathcal{S}\sigma(\mathbf{x}_{lm}) = \int_{\gamma \setminus \{\gamma_{l-1} \cup \gamma_l \cup \gamma_{l+1}\}} g(\mathbf{x}_{lm}, \mathbf{y}) \sigma(\mathbf{y}) ds_{\mathbf{y}} + \int_{\gamma_{l-1} \cup \gamma_l \cup \gamma_{l+1}} g(\mathbf{x}_{lm}, \mathbf{y}) \sigma(\mathbf{y}) ds_{\mathbf{y}}, \quad (37)$$

where γ_l denotes the l th panel.

For integration on non-adjacent panels, namely, the first integral in the right hand side of (37), we simply set $w_{lmij} = w_{ij}$, where w_{ij} is the standard scaled Gauss-Legendre weight on panel i . Therefore, for non-adjacent panels, the order of accuracy is expected to be $2p - 1$, although rigorous analysis and error estimates require knowledge of the regularity of the density function σ .

For panels that are adjacent or self-interacting with γ_l , i.e., $\gamma_{l-1} \cup \gamma_l \cup \gamma_{l+1}$, it is difficult to derive efficient, high-order accurate Nyström schemes in which the quadrature nodes are the same as the discretization nodes (i.e. the points at which σ are sampled, the p Gauss-Legendre nodes on each panel). Often it can be very beneficial to use additional or at least different quadrature *support nodes* for approximating the integral. These support nodes and corresponding weights in our case were computed using the scheme of [8]. More specifically, to compute the integral over panel γ_i , for $i = l - 1, l, l + 1$, at a target \mathbf{x}_{lm} , we approximate as

$$\int_{\gamma_i} g(\mathbf{x}_{lm}, \mathbf{y}) \sigma(\mathbf{y}) ds_{\mathbf{y}} \approx \sum_{j=1}^p c_{ij} \int_{\gamma_i} g(\mathbf{x}_{lm}, \mathbf{y}) P_j^i(\mathbf{y}) ds_{\mathbf{y}} \approx \sum_{j=1}^p c_{ij} I_j(\mathbf{x}_{lm}), \quad (38)$$

where P_j^i is the scaled Legendre polynomial of degree $j - 1$ on panel γ_i and c_{ij} are the Legendre expansion coefficients of the degree $j - 1$ interpolating polynomial for σ . For a fixed \mathbf{x}_{lm} , each $I_j(\mathbf{x}_{lm})$ contains no unknowns and can be evaluated via a pre-computed high-order generalized Gaussian quadrature. The number of nodes required in these quadratures may vary. Details on generating these quadratures were discussed in [8], and an analogous Nyström-like discretization scheme along surfaces in three dimensions was discussed in [7].

Furthermore, note that each c_{ij} can be obtained via application of a $p \times p$ transform matrix acting on values of σ . Denote this transform matrix as \mathbf{U}^i , and it's entries as U_{jn}^i . Inserting this into (38), we have

$$\int_{\gamma_i} g(\mathbf{x}_{lm}, \mathbf{y}) \sigma(\mathbf{y}) ds_{\mathbf{y}} \approx \sum_{j=1}^p \sum_{n=1}^p U_{jn}^i \sigma(\mathbf{y}_{in}) I_j(\mathbf{x}_{lm}) = \sum_{n=1}^p \left(\sum_{j=1}^p U_{jn}^i I_j(\mathbf{x}_{lm}) \right) \sigma(\mathbf{y}_{in}). \quad (39)$$

By simply exchanging the indexes n and j , we obtain

$$\int_{\gamma_i} g(\mathbf{x}_{lm}, \mathbf{y}) \sigma(\mathbf{y}) ds_{\mathbf{y}} \approx \sum_{j=1}^p \left(\sum_{n=1}^p U_{nj}^i I_n(\mathbf{x}_{lm}) \right) \sigma(\mathbf{y}_{ij}), \quad (40)$$

which implies we can take $w_{lmij} g(\mathbf{x}_{lm}, \mathbf{y}_{ij}) \approx \sum_{n=1}^p U_{nj}^i I_n(\mathbf{x}_{lm})$ to approximate the second part of the singular integral (37).

In the case that γ is only piecewise smooth, a graded mesh near the corner is used to maintain high-order accuracy. That is, after uniform discretization of each smooth component of γ , we perform a dyadic refinement on panels that impinge on each corner point. Then we apply the p th order generalized Gaussian quadrature on each of the refined panels. This procedure, along with proper quadrature weighting, has been shown to achieve high-order accuracy for curves with corners [6, 29].

6. NUMERICAL EXAMPLES

In this section, we apply our algorithm to computing elastic scattering from various elastically rigid axisymmetric objects. In order to verify the accuracy of our algorithm, we choose to test the extinction theorem by solving the integral formulation (12) with an artificial solution. Specifically,

we let the incident field in the exterior of Ω be generated by a polarized point source $\Phi(\mathbf{x}, \mathbf{y}_0)$ with \mathbf{y}_0 located inside Ω , i.e.

$$\mathbf{u}^{\text{inc}}(\mathbf{x}) = -\Phi(\mathbf{x}, \mathbf{y}_0)\mathbf{p}, \quad (41)$$

where

$$\Phi(\mathbf{x}, \mathbf{y}_0) = \frac{1}{\mu} \left(G^{\kappa_s}(\mathbf{x}, \mathbf{y}_0)\mathbf{I} + \frac{1}{\kappa_s^2} \nabla_{\mathbf{x}}^T \nabla_{\mathbf{x}} (G^{\kappa_s}(\mathbf{x}, \mathbf{y}_0) - G^{\kappa_p}(\mathbf{x}, \mathbf{y}_0)) \right) \quad (42)$$

is the the fundamental solution of the Navier equation [39], \mathbf{I} is the 3×3 identity matrix, and \mathbf{p} is the polarization vector. Since the incident field generated by the polarized point source satisfies the elastic equation in $\mathbb{R}^3 \setminus \overline{\Omega}$ with radiation condition, by extinction theorem, the scattered field is simply given by

$$\mathbf{u}^{\text{sc}}(\mathbf{x}) = \Phi(\mathbf{x}, \mathbf{y}_0)\mathbf{p}.$$

Therefore, if the boundary condition on Γ is specified by \mathbf{u}^{inc} , by uniqueness, we should recover the field $\mathbf{u}^{\text{sc}}(\mathbf{x})$ by solving equation (12). Throughout all the numerical examples, we let the source \mathbf{y}_0 be $(0.1, 0.1, 0.1)$ with $\mu = 1$ and $\mathbf{p} = (1, 0, 0)^T$.

In addition, we also solve the integral formulation (12) with an incident plane wave:

$$\mathbf{u}^{\text{inc}}(\mathbf{x}) = (\mathbf{d} \cdot \mathbf{p})\mathbf{d}e^{i\kappa_p \mathbf{d} \cdot \mathbf{x}} + (\mathbf{d} \times \mathbf{p}) \times \mathbf{d}e^{i\kappa_s \mathbf{d} \cdot \mathbf{x}}, \quad (43)$$

where \mathbf{d} is the propagation direction and $\mathbf{d} \times \mathbf{p}$ is an orthogonal polarization vector. Throughout all the examples, we let

$$\begin{aligned} \mathbf{d} &= (\cos \theta_1 \sin \varphi_1, \sin \theta_1 \sin \varphi_1, \cos \varphi_1), \\ \mathbf{p} &= (\cos \theta_2 \sin \varphi_2, \sin \theta_2 \sin \varphi_2, \cos \varphi_2), \end{aligned} \quad (44)$$

with $\theta_1 = \pi/4$, $\varphi_1 = \pi/8$, $\theta_2 = \pi/5$, and $\varphi_2 = \pi/10$. The far field pattern of the scattered wave can be found by letting $|\mathbf{x}| \rightarrow \infty$ in (11) and using the asymptotic form of the Green's function (9):

$$\mathbf{u}^\infty(\theta, \varphi) = -\frac{1}{4\pi} \left(\int_{\Gamma} \nabla_{\mathbf{y}} e^{-i\kappa_p \hat{\mathbf{x}} \cdot \mathbf{y}} \sigma(\mathbf{y}) ds(\mathbf{y}) + \int_{\Gamma} \nabla_{\mathbf{y}} e^{-i\kappa_s \hat{\mathbf{x}} \cdot \mathbf{y}} \times \mathbf{J}(\mathbf{y}) ds(\mathbf{y}) \right), \quad (45)$$

where $\theta \in [0, 2\pi]$ is the azimuthal angle, $\varphi \in [0, \pi]$ is the angle with respect to the positive z axis, and $\hat{\mathbf{x}} = (\cos \theta \sin \varphi, \sin \theta \sin \varphi, \cos \varphi)$ is a point on the unit sphere.

We make use of the following notations in the subsequent tables that present data from our scattering experiments:

- κ_p : the compressional wavenumber,
- κ_s : the shear wavenumber,
- N_f : the number of Fourier modes in the azimuthal direction used to resolve the solution. In other words, the Fourier modes are $-N_f, -N_f + 1, \dots, N_f - 1, N_f$.
- N_{pts} : the total number of points used to discretize γ ,
- T_{matgen} : the time (secs.) to construct the relevant matrix entries for all integral equations,
- T_{solve} : the time (secs.) to compute the **LU**-factorization of the system matrices for all modes,
- T_{syn} : the time (secs.) to synthesize the density and surface current from their Fourier modes,
- E_{error} : the absolute L^2 error of the elastic field measured at points placed on a sphere that encloses Ω .

The accuracy that controls the kernel evaluation (i.e. where to truncate Fourier coefficients in the discrete convolutions) and the number of Fourier modes in the decomposition of the incident wave is set to be 1×10^{-12} . We apply the Nyström-like discretization described earlier in Section 5 to discretize the line integral equations with $p = 30$ on each panel. In other words, we use 30th-order generalized Gaussian quadrature rules which contain 30 support nodes and weights for self-interacting panels (which vary according to the location of the target) and 56 support nodes and weights on adjacent panels (which are target independent). All experiments were implemented in FORTRAN 90 and carried out on a laptop with four 2.0Ghz Intel cores and 16Gb of RAM.

We made use of OPENMP for parallelism across decoupled Fourier modes, and simple block LU -factorization using LAPACK for matrix inversion. Various fast direct solvers such as [18, 30, 33, 37] could be applied if larger problems were involved.

Lastly, it is generally difficult to analytically parameterize the generating curve with respect to arclength. In the following examples, we have discretized the generating curve at panel-wise Gauss-Legendre points in some parameter t , not necessarily arclength. Any previous formulae which assumed arclength can be easily adjusted with factors of ds/dt to account for the parameterization metric.

Remark 6.1. *The examples we tested here are all for the elastic scattering of a single object. The algorithm, however, can be extended to the scattering of multiple axisymmetric objects by transforming the incident field into the local coordinate of each object [19, 23]. In particular, we may use FMM developed for acoustic and Maxwell equations to accelerate the scattering among multi-particles, as presented in [35] for the two dimensional case. This will be explored in our future investigation.*

Example 1: Scattering from a sphere. Consider a sphere with the generating curve given by

$$r(t) = 2 \sin(t), \quad z(t) = 2 \cos(t), \quad t \in [0, \pi]. \quad (46)$$

We solve the scattering problem of the sphere at several wavenumbers, with accuracy results shown in Table 1. By using at least 12 points per wavelength, we are able to achieve 8 digits of accuracy for most of the cases. Note that the CPU time is dominated by the generation of matrix elements, which roughly scales quadratically with the number of unknowns. For the same number of unknowns, the computational time depends linearly on the number of Fourier modes. Although the linear system for each mode is decoupled from the other modes, which makes parallelization straightforward, the computational time T_{solve} presented in Table 1 is the total matrix inversion time via sequential solve. Despite its $\mathcal{O}(N_f N_{pts}^3)$ complexity, it is still much smaller than T_{matgen} . Similar phenomenon has been observed in [36] for the electromagnetic scattering from penetrable axisymmetric bodies. The time to synthesize the charge and current from their modes, as can be done by FFT, is negligible compared to the other parts during the solve. In addition, once the matrix is factorized, additional solves for new right hand sides are very fast.

For an incident plane wave with wavenumber $\kappa_p = 10$ and $\kappa_s = 20$. Figure 1(A) shows the imaginary part of the x component of the scattered field \mathbf{u}^{sc} in Cartesian coordinates, which is denoted by $\Im \mathbf{u}_1^{sc}$, at the hemisphere with radius 4. Figure 1(B) shows the imaginary part of the far field pattern, denoted by $\Im \mathbf{u}_1^\infty$. Figure 1(C) plots the pointwise error for the point source scattering by comparing the numerical solution with the exact solution at the hemisphere. We can see that 9 digits accuracy is obtained for the elastic scattering from a sphere.

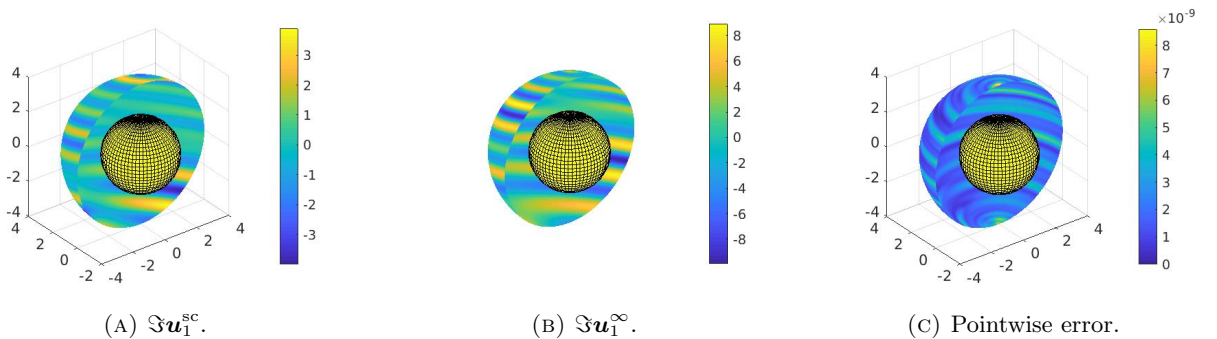


FIGURE 1. Elastic scattering of a sphere with wavenumber $\kappa_p = 10.0$ and $\kappa_s = 20.0$.

TABLE 1. Results for the elastic scattering of a sphere at different wavenumber.

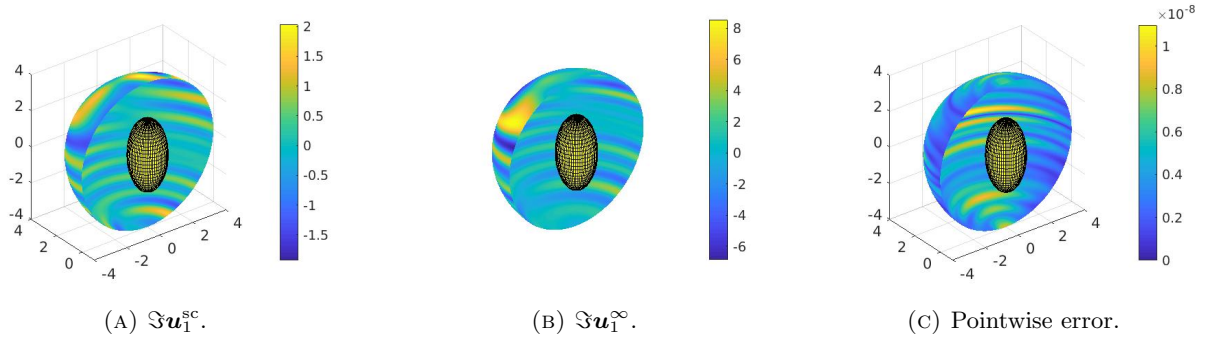
κ_p	κ_s	N_f	N_{pts}	$T_{matgen}(s)$	$T_{solve}(s)$	T_{syn}	E_{error}
1	2	12	120	2.33E+0	1.82E-1	6.55E-2	1.14E-11
1	5	12	180	5.37E+0	4.18E-1	9.70E-2	8.51E-11
1	10	15	240	9.65E+0	9.46E-1	1.53E-1	3.82E-9
5	2	11	180	5.38E+0	3.76E-1	8.68E-2	1.59E-10
5	10	14	240	9.41E+0	9.01E-1	1.45E-1	2.27E-10
5	20	18	300	1.83E+1	1.98E+0	2.52E-1	3.99E-9
10	5	14	240	9.96E+0	9.19E-1	1.48E-1	3.41E-10
10	20	18	300	1.81E+1	1.97E+0	2.48E-1	4.96E-9
10	40	24	480	5.88E+1	8.70E+0	5.77E-1	1.84E-8
20	5	17	300	1.78E+1	1.89E+0	2.39E-1	1.26E-9
20	10	17	300	1.81E+1	1.87E+0	2.37E-1	1.76E-9
20	40	24	480	6.13E+1	8.63E+0	5.43E-1	1.37E-8

Example 2: Scattering from an ellipsoid. We next consider scattering from an ellipsoid whose generating curve is given by

$$r(t) = \sin(t), \quad z(t) = 2 \cos(t), \quad t \in [0, \pi]. \quad (47)$$

The results are comparable with the sphere case. As we can see from Table 2, at small wavenumber, we obtain approximately 10 digits of accuracy. The accuracy slowly deteriorates to 7 digits as the wavenumber increases. This is due to a stronger singularity near the poles (at $t = 0$ and $t = 1$) for higher wavenumbers. More digits can be obtained if additional refinement were implemented. Once again, if the system is factored, additional solves for new right-hand sides are inexpensive. This can be applied, for instance, to efficiently solving the elastic scattering problem with multiple incidences.

For an incident plane wave with $\kappa_p = 10.0$ and $\kappa_s = 20.0$, Figure 2(A) and (B) plot the imaginary parts of the x component of the scattered elastic field and the far field pattern, respectively. Figure 2(C) shows the pointwise error for point source scattering by comparing with the exact solution. One can see that 8 digits accuracy is obtained by roughly 20 points per wavelength.

FIGURE 2. Elastic scattering of an ellipsoid with wavenumber $\kappa_p = 10.0$ and $\kappa_s = 20.0$.

Example 3: Scattering from a rotated starfish. For the third example, we consider an axisymmetric object whose generating curve is given by

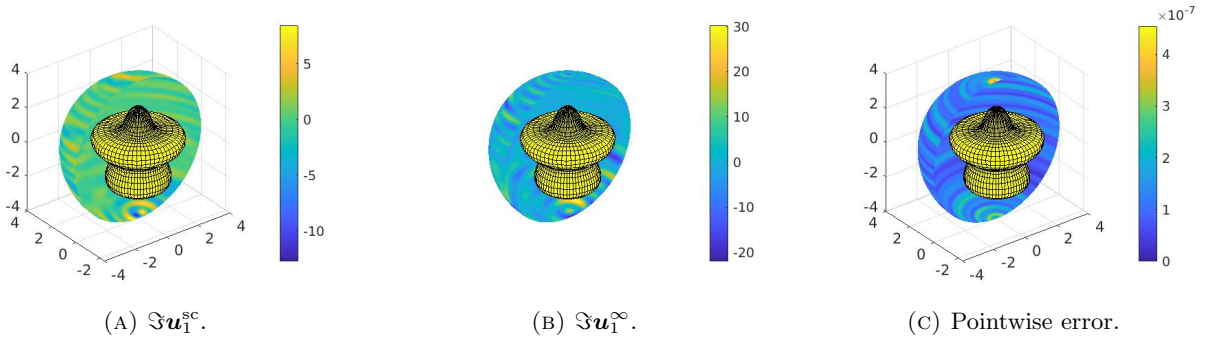
$$\begin{aligned} r(t) &= [2 + 0.5 \cos(5\pi(t - 1))] \cos(\pi(t - 0.5)), \\ z(t) &= [2 + 0.5 \cos(5\pi(t - 1))] \sin(\pi(t - 0.5)), \end{aligned} \quad (48)$$

TABLE 2. Results for the elastic scattering of an ellipsoid at different wavenumber.

κ_p	κ_s	N_f	N_{pts}	$T_{matgen}(s)$	$T_{solve}(s)$	T_{syn}	E_{error}
1	2	16	120	2.35E+0	2.32E-1	9.23E-2	3.55E-12
1	5	16	180	5.60E+0	5.19E-1	1.44E-1	6.79E-11
1	10	16	240	9.52E+0	1.07E+0	2.01E-1	4.58E-10
5	2	15	180	5.55E+0	5.41E-1	1.15E-1	2.11E-10
5	10	16	240	9.56E+0	1.04E+0	1.83E-1	2.92E-10
5	20	19	300	1.69E+1	2.07E+0	2.59E-1	3.81E-9
10	5	15	240	9.38E+0	9.63E-1	1.53E-1	2.53E-9
10	20	18	300	1.65E+1	1.97E+0	2.50E-1	4.89E-9
10	40	24	480	5.40E+1	8.66E+0	5.77E-1	9.79E-8
20	5	18	300	1.71E+1	2.09E+0	2.53E-1	2.45E-9
20	10	18	300	1.68E+1	1.98E+0	2.53E-1	1.75E-9
20	40	24	480	5.77E+1	8.65E+0	5.82E-1	7.37E-8

for $t \in [0, 1]$. The generating curve is open but gives rise to a smooth surface when crossing the z -axis. We refer to this object as the rotated *starfish*, as shown in Figure 3. We therefore apply a uniform panel discretization to the parameter space $[0, 1]$. Table 3 provides the accuracy results for various wavenumbers and discretization refinements. We obtain 7 to 9 digits of accuracy by using a sufficient number of discretization points per wavelength. The computational time is again dominated by the matrix generation, T_{matgen} . As the matrix is generated and factored, the time for additional solves is negligible.

Figure 3(A) shows the scattering results with a plane wave incidence for $\kappa_p = 10$ and $\kappa_s = 20$. The far field pattern is given in 3(B). Pointwise error for point source scattering is shown in 3(C). Roughly 7 digits accuracy is obtained for all the points on the hemisphere with radius 4.

FIGURE 3. Elastic scattering of a rotated *starfish* with wavenumber $\kappa_p = 10.0$ and $\kappa_s = 20.0$.

Example 4: Scattering from a droplet. In this example, we consider the scattering of a droplet with parametrization of the generating curve given by

$$\begin{aligned} r(t) &= 4 \sin(\pi t) \cos[0.5\pi(t - 1.5)], \\ z(t) &= 4 \sin(\pi t) \sin[0.5\pi(t - 1.5)] + 2, \end{aligned} \quad (49)$$

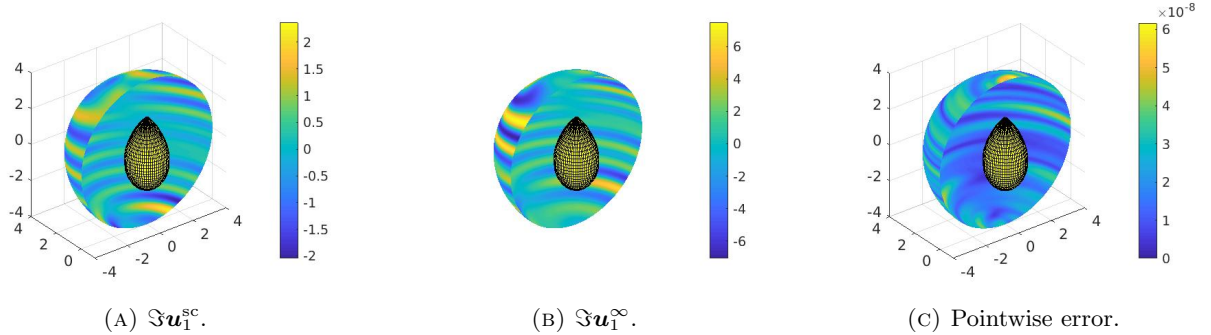
for $t \in [0.5, 1]$. It has a point singularity at $t = 1$, as shown by Figure 4. To resolve this singularity, we first apply a uniform panel discretization to the parameter space $[0.5, 1]$. Then for the two panels that are adjacent to the singular point, we apply four times dyadic refinement, which yields a graded mesh. The scattering result for a point source at different wavenumber is given in Table 4. The

TABLE 3. Results for the elastic scattering of a rotated *starfish* at different wavenumber.

κ_p	κ_s	N_f	N_{pts}	$T_{matgen}(s)$	$T_{solve}(s)$	T_{syn}	E_{error}
1	2	13	300	1.52E+1	1.46E+0	1.68E-1	2.06E-10
1	5	13	360	2.13E+1	2.28E+0	2.05E-1	2.95E-10
1	10	16	420	3.31E+1	3.75E+0	2.63E-1	1.72E-8
5	2	12	360	2.07E+1	2.11E+0	1.91E-1	1.66E-9
5	10	15	420	3.35E+1	3.73E+0	2.63E-1	2.14E-8
5	20	18	480	4.87E+1	6.34E+0	4.54E-1	1.63E-7
10	5	14	420	3.23E+1	3.47E+0	2.51E-1	1.14E-9
10	20	18	480	4.88E+1	6.38E+0	4.53E-1	2.55E-7
10	40	24	600	1.04E+2	1.63E+1	7.12E-1	3.05E-7
20	5	17	480	4.72E+1	6.06E+0	4.44E-1	1.01E-7
20	10	17	480	4.76E+1	6.06E+0	4.37E-1	1.25E-7
20	40	24	600	1.04E+2	1.68E+1	7.09E-1	3.16E-7

table shows more than 7 digits accuracy for the scattering at various wavenumber, which implies the point singularity of the droplet is fully resolved.

Similarly, we give the scattering result with a plane wave incidence for $\kappa_p = 10$ and $\kappa_s = 20$ in Figure 4(A) and (B). Figure 4(C) shows that 8 digits accuracy can be obtained for point source scattering. This is done in less than one minute computational time, which demonstrates the efficiency of our solver.

FIGURE 4. Elastic scattering of a droplet with wavenumber $\kappa_p = 10.0$ and $\kappa_s = 20.0$.

7. CONCLUSION

In this paper, we provided a derivation of the boundary integral equation for the elastic scattering from a three dimensional rigid obstacle in isotropic media based on Helmholtz decomposition. Even though the resulting integral equation system is not second-kind (see [35] for discussions in two dimensional case), it remains relatively well-conditioned even when the boundary has a modest number of edges or geometric singularities. Our numerical algorithm strongly takes advantage of the axisymmetric geometry by using a Fourier-based separation of variables in the azimuthal angle to obtain a sequence of decoupled integral equations on a cross section of the geometry. Using FFTs, we are able to efficiently evaluate the modal Green's functions and their derivatives. High-order accurate convergence is observed when discretizing the integral equations using generalized Gaussian quadratures and an adaptive Nyström-like method. Numerical examples show that the algorithm can efficiently and accurately solve the scattering problem from various axisymmetric objects, even in the presence of corner singularities. Extension of this work to multi-particle scattering, as well

TABLE 4. Results for the elastic scattering of a droplet at different wavenumber.

κ_p	κ_s	N_f	N_{pts}	$T_{matgen}(s)$	$T_{solve}(s)$	T_{syn}	E_{error}
1	2	16	300	1.66E+1	1.91E+0	2.40E-1	2.38E-10
1	5	15	360	2.24E+1	2.56E+0	2.28E-1	3.14E-9
1	10	16	420	3.38E+1	4.02E+0	3.14E-1	3.26E-8
5	2	15	360	2.25E+1	2.57E+0	2.30E-1	1.68E-9
5	10	16	420	3.41E+1	3.98E+0	3.12E-1	2.57E-8
5	20	19	480	4.78E+1	6.65E+0	4.63E-1	4.22E-8
10	5	15	420	3.33E+1	3.73E+0	2.69E-1	3.43E-9
10	20	19	480	4.81E+1	6.69E+0	4.63E-1	3.42E-8
10	40	24	600	9.82E+1	1.65E+1	6.98E-1	9.11E-8
20	5	18	480	4.68E+1	6.33E+0	4.51E-1	1.38E-8
20	10	18	480	4.69E+1	6.33E+0	4.49E-1	1.48E-8
20	40	24	600	9.55E+1	1.66E+1	6.93E-1	3.61E-7

as the applications to inverse elastic scattering are still under investigation. We will report them in the future.

APPENDIX A. FOURIER EXPANSION FOR THE SURFACE GRADIENT AND DIVERGENCE

Let Γ be the boundary of a three dimensional axisymmetric object with parametrization given by

$$(r(s) \cos \theta, r(s) \sin \theta, z(s)),$$

and $(\boldsymbol{\tau}_1, \boldsymbol{\tau}_2)$ be the unit tangential vectors on Γ . Here we do not require the parameter s to be arclength of the generating curve of Γ .

Lemma A.1. *The surface gradient of a function $\sigma \in C^{1,\alpha}(\Gamma)$ with Fourier expansion (19) is given by*

$$\text{Grad} \sigma = \sum_m \left(\frac{1}{\sqrt{r'^2 + z'^2}} \frac{\partial \sigma_m}{\partial s} \boldsymbol{\tau}_1 + \frac{im}{r} \sigma_m \boldsymbol{\tau}_2 \right) e^{im\theta}. \quad (50)$$

The surface divergence of a tangential vector $\mathbf{J} = J^1 \boldsymbol{\tau}_1 + J^2 \boldsymbol{\tau}_2 \in T_d^{0,\alpha}(\Gamma)$ with Fourier expansion (20) is given by

$$\text{Div} \mathbf{J} = \sum_m \left(\frac{1}{r\sqrt{r'^2 + z'^2}} (r'(s)J_m^1 + r(J_m^1)') + \frac{im}{r} J_m^2 \right) e^{im\theta}. \quad (51)$$

We first give the expression for $\text{Grad}_{\mathbf{y}}(\mathbf{n}(\mathbf{x}) \cdot \mathbf{n}(\mathbf{y}))$ and $\text{Div}_{\mathbf{y}}(\mathbf{n}(\mathbf{y}) \times \boldsymbol{\tau}_i(\mathbf{x}) \times \mathbf{n}(\mathbf{y}))$, $i = 1, 2$. Since

$$\begin{aligned} \mathbf{n}(\mathbf{x}) &= C_t (z'(t)(\cos \theta_t, \sin \theta_t, 0) - r'(t)(0, 0, 1)), \\ \mathbf{n}(\mathbf{y}) &= C_s (z'(s)(\cos \theta, \sin \theta, 0) - r'(s)(0, 0, 1)), \end{aligned}$$

where $C_s = 1/\sqrt{r'(s)^2 + z'(s)^2}$, $C_t = 1/\sqrt{r'(t)^2 + z'(t)^2}$, it holds

$$\begin{aligned} &\text{Grad}_{\mathbf{y}}(\mathbf{n}(\mathbf{x}) \cdot \mathbf{n}(\mathbf{y})) \\ &= C_s (C_t C'_s (z'(t)z'(s) \cos(\theta_t - \theta) + r'(t)r'(s)) + C_t C_s (z'(t)z''(s) \cos(\theta_t - \theta) + r'(t)r''(s))) \boldsymbol{\tau}_1 \\ &+ 1/r(s) C_t C_s z'(t)z'(s) \sin(\theta_t - \theta) \boldsymbol{\tau}_2. \end{aligned}$$

Similarly, since

$$\begin{aligned} \boldsymbol{\tau}_1(\mathbf{x}) &= C_t (r'(t)(\cos \theta_t, \sin \theta_t, 0) + z'(t)(0, 0, 1)), & \boldsymbol{\tau}_2(\mathbf{x}) &= (-\sin \theta_t, \cos \theta_t, 0), \\ \boldsymbol{\tau}_1(\mathbf{y}) &= C_s (r'(s)(\cos \theta, \sin \theta, 0) + z'(s)(0, 0, 1)), & \boldsymbol{\tau}_2(\mathbf{y}) &= (-\sin \theta, \cos \theta, 0), \end{aligned}$$

by Lemma A.1, it holds

$$\begin{aligned}
& \operatorname{Div}_{\mathbf{y}}(\mathbf{n}(\mathbf{y}) \times \boldsymbol{\tau}_1(\mathbf{x}) \times \mathbf{n}(\mathbf{y})) \\
&= C_s/r(s) [r'(s)C_t C_s(r'(t)r'(s) \cos(\theta_t - \theta) + z'(t)z'(s)) \\
&+ r(s)C_t C_s'(r'(t)r'(s) \cos(\theta_t - \theta) + z'(t)z'(s)) \\
&+ r(s)C_t C_s(r'(t)r''(s) \cos(\theta_t - \theta) + z'(t)z''(s))] \\
&- 1/r(s)C_t r'(t) \cos(\theta_t - \theta),
\end{aligned}$$

and

$$\begin{aligned}
& \operatorname{Div}_{\mathbf{y}}(\mathbf{n}(\mathbf{y}) \times \boldsymbol{\tau}_2(x) \times \mathbf{n}(\mathbf{y})) \\
&= C_s/r(s) [-r'(s)C_s r'(s) \sin(\theta_t - \theta) - r(s)(C_s' r'(s) + C_s r''(s)) \sin(\theta_t - \theta)] \\
&+ 1/r(s) \sin(\theta_t - \theta).
\end{aligned}$$

To numerically construct the surface gradient operator for an unknown function σ , we make use of the fact that σ is discretized on p scaled Gauss-Legendre nodes on each panel as discussed in Section 5. Following the notation in Section 5, σ on the i th panel γ_i is approximated by

$$\sigma(\mathbf{y}) \approx \sum_{j=1}^p c_{ij} P_j^i(\mathbf{y}) = \sum_{j=1}^p \sum_{n=1}^p U_{jn}^i \sigma(\mathbf{y}_{in}) P_j^i(\mathbf{y}).$$

Therefore the surface divergence can be approximated as

$$\operatorname{Grad}_{\mathbf{y}} \sigma(\mathbf{y}) \approx \sum_{j=1}^p \sum_{n=1}^p U_{jn}^i \sigma(\mathbf{y}_{in}) \operatorname{Grad}_{\mathbf{y}} P_j^i(\mathbf{y}) = \sum_{n=1}^p \sum_{j=1}^p U_{jn}^i \operatorname{Grad}_{\mathbf{y}} P_j^i(\mathbf{y}) \sigma(\mathbf{y}_{in}).$$

By taking \mathbf{y} to be the p scaled Gauss-Legendre nodes on the i th panel, we obtain the discretized surface gradient operator for σ . The discretization of surface divergence operator for a vector function \mathbf{J} can be similarly constructed.

Combining the results above with Lemmas 4.1 and 4.2, we are able to obtain the azimuthal Fourier decomposition of boundary operators \mathcal{H} and \mathcal{N} . Details are omitted.

REFERENCES

- [1] Ahner, J.F., Hsiao, G.C.: On the two-dimensional exterior boundary-value problems of elasticity. *SIAM J. Appl. Math.* **31**, 677–685 (1976)
- [2] Alpert, B.: Hybrid Gauss-trapezoidal quadrature rules. *SIAM J. Sci. Comput.* **20**(5), 1551–1584 (1999)
- [3] Ammari, H., Bretin, E., Garnier, J., Kang, H., Lee, H., Wahab, A.: *Mathematical Methods in Elasticity Imaging*. Princeton University Press, New Jersey (2015)
- [4] Bao, G., Xu, L., Yin, T.: An accurate boundary element method for the exterior elastic scattering problem in two dimensions. *J. Comput. Phys.* **348**, 343–363 (2017)
- [5] Borges, C., Lai, J.: Inverse scattering reconstruction of a three dimensional sound-soft axis-symmetric impenetrable object. *Inverse Prob.* **36**(10), 105005 (2020)
- [6] Bremer, J.: On the Nyström discretization of integral equations on planar curves with corners. *Appl. Comput. Harm. Anal.* **32**, 45–64 (2012)
- [7] Bremer, J., Gimbutas, Z.: A Nyström method for weakly singular integral operators on surfaces. *J. Comput. Phys.* **231**(14), 4885–4903 (2012)
- [8] Bremer, J., Gimbutas, Rokhlin, V.: A nonlinear optimization procedure for generalized Gaussian quadratures. *SIAM J. Sci. Comput.* **32**(4), 1761–1788 (2010)
- [9] Bu, F., Lin, J., Reitich, F.: A fast and high-order method for the three-dimensional elastic wave scattering problem. *J. Comput. Phys.* **258**, 856–870 (2014)
- [10] Cohl, H.S., Tohline, J.E.: A compact cylindrical Green’s function expansion for the solution of potential problems. *Astrophys. J.* **527**(1), 86–101 (1999)
- [11] Conway, J.T., Cohl, H.S.: Exact Fourier expansion in cylindrical coordinates for the three-dimensional Helmholtz Green function. *Z. Angew. Math. Phys.* **61**, 425–442 (2010)

- [12] Colton, D., Kress, R.: Inverse Acoustic and Electromagnetic Scattering Theory, 3rd edition. Springer, New York (2013)
- [13] Dong, H., Lai, J., Li, P.: Inverse obstacle scattering for elastic waves with phased or phaseless far-field data. *SIAM J. Imaging Sci.* **12**, 809–838 (2019)
- [14] Dong, H., Lai, J., Li, P.: An inverse acoustic-elastic interaction problem with phased or phaseless far-field data. *Inverse Probl.* **36**, 035014 (2020)
- [15] Dong, H., Lai, J., Li, P.: A highly accurate boundary integral method for the elastic obstacle scattering problem. *Math. Comput.* *to appear*, arXiv:2007.08808
- [16] Epstein, C.L., Greengard, L., O’Neil, M.: A high-order wideband direct solver for electromagnetic scattering from bodies of revolution. *J. Comput. Phys.* **387**, 205–229 (2019)
- [17] Geng, N., Carin, L.: Wide-band electromagnetic scattering from a dielectric BOR buried in a layered lossy dispersive medium. *IEEE Trans. Antennas Propag.* **47**(4), 610–619 (1999)
- [18] Gillman, A., Young, P.M., Martinsson, P.G.: A direct solver with $O(N)$ complexity for integral equations on one-dimensional domains. *Front. Math. China* **7**(2), 217–247 (2012)
- [19] Gimbutas, Z., Greengard, L.: Fast multi-particle scattering: A hybrid solver for the Maxwell equations in microstructured materials. *J. Comput. Phys.* **232**, 22–32 (2013)
- [20] Greengard, L., O’Neil, M., Rachh, M., Vico, F.: Fast multipole methods for evaluation of layer potentials with locally-corrected quadratures. Submitted, arXiv:2006.02545
- [21] Greengard, L., Rokhlin, V.: A fast algorithm for particle simulations. *J. Comput. Phys.* **73**, 325–348 (1987)
- [22] Gustafsson, M.: Accurate and efficient evaluation of modal green’s functions. *J. Electromagnet. Wave.* **24**(10), 1291–1301 (2010)
- [23] Hao, S., Barnett, A.H., Martinsson, P.G., Young, P.: High-order accurate Nyström discretization of integral equations with weakly singular kernels on smooth curves in the plane. *Adv. Comput. Math.* **40**, 245–272 (2014)
- [24] Hao, S., Martinsson, P.G., Young, P.: An efficient and highly accurate solver for multi-body acoustic scattering problems involving rotationally symmetric scatterers. *Comput. Math. Appl.* **69**, 304–318 (2015)
- [25] Helsing, J., Holst, A.: Variants of an explicit kernel-split panel-based Nyström discretization scheme for Helmholtz boundary value problems. *Adv. Comput. Math.* **41**, 691–708 (2015)
- [26] Helsing, J., Karlsson, A.: An explicit kernel-split panel-based Nyström scheme for integral equations on axially symmetric surfaces. *J. Comput. Phys.* **272**, 686–703 (2014)
- [27] Helsing, J., Karlsson, A.: Determination of normalized electric eigenfields in microwave cavities with sharp edges. *J. Comput. Phys.* **304**(Supplement C), 465–486 (2016)
- [28] Helsing, J., Karlsson, A.: Resonances in axially symmetric dielectric objects. *IEEE Trans. Microw. Theory Tech.* **65**(7), 2214–2227 (2017)
- [29] Helsing, J., Ojala, R.: Corner singularities for elliptic problems: Integral equations, graded meshes, quadrature, and compressed inverse preconditioning. *J. Comput. Phys.* **227**, 8820–8840 (2008)
- [30] Ho, K.L., Greengard, L.: A fast direct solver for structured linear systems by recursive skeletonization. *SIAM J. Sci. Comput.*, 34(5):2507–2532, 2012.
- [31] G. Hu, A. Kirsch, and M. Sini, *Some inverse problems arising from elastic scattering by rigid obstacles*, *Inverse Probl.* **29**, 015009 (2013)
- [32] Kress, R.: Linear Integral Equations. Springer, New York (1999)
- [33] Lai, J., Ambikasaran, S., Greengard, L.F.: A Fast Direct Solver for High Frequency Scattering from a Large Cavity in Two Dimensions. *SIAM J. Sci. Comput.* **36**(6), B887–B903, (2014)
- [34] Lai, J., Greengard, L., O’Neil, M.: Robust integral formulations for electromagnetic scattering from three-dimensional cavities. *J. Comput. Phys.* **345**, 1–16 (2017)
- [35] Lai, J., Li, P.: A framework for simulation of multiple elastic scattering in two dimensions. *SIAM J. Sci. Comput.* **41**, A3276–A3299 (2019)
- [36] Lai, J., O’Neil, M.: An FFT-accelerated direct solver for electromagnetic scattering from penetrable axisymmetric objects. *J. Comput. Phys.* **390**, 152–174 (2019)
- [37] Liu, Y., Barnett, A.H.: Efficient numerical solution of acoustic scattering from doubly-periodic arrays of axisymmetric objects. *J. Comput. Phys.* **324**, 226–245 (2016)
- [38] Louër, F.L.: On the Fréchet derivative in elastic obstacle scattering. *SIAM J. Appl. Math.* **72**, 1493–1507 (2012)
- [39] Louër, F.L.: A high order spectral algorithm for elastic obstacle scattering in three dimensions. *J. Comput. Phys.* **279**, 1–17 (2014)
- [40] O’Neil, M., Cerfon, A.J.: An integral equation-based numerical solver for Taylor states in toroidal geometries. *J. Comput. Phys.* **359**, 263–282 (2018)
- [41] Pao, Y.H., Varatharajulu, V.: Huygens’ principle, radiation conditions, and integral formulas for the scattering of elastic waves. *J. Acoust. Soc. Amer.* **59**, 1361–1371 (1976)
- [42] Tong, M.S., Chew, W.C.: Nyström method for elastic wave scattering by three-dimensional obstacles. *J. Comput. Phys.* **226**, 1845–1858 (2007)

- [43] Young, P., Hao, S., Martinsson, P.G.: A high-order Nyström discretization scheme for boundary integral equations defined on rotationally symmetric surfaces. *J. Comput. Phys.* **231**(11), 4142–4159 (2012)
- [44] Yu, W.M., Fang, D.G., Cui, T.J.: Closed form modal green's functions for accelerated computation of bodies of revolution. *IEEE Trans. Antennas Propag.* **56**(11), 3452–3461 (2008)

SCHOOL OF MATHEMATICAL SCIENCES, ZHEJIANG UNIVERSITY, HANGZHOU, ZHEJIANG 310027, CHINA

Email address: laijun6@zju.edu.cn

SCHOOL OF MATHEMATICS, JILIN UNIVERSITY, CHANGCHUN, JILIN 130012, CHINA

Email address: dhp@jlu.edu.cn